Superior resolution through multiparameter FWI imaging: A new philosophy in seismic processing and imaging

James McLeman[1], Tom Rayment[2], Tim Burgess[1], Karen Dancer[1], Gary Hampson[2], and Alex Pauli[1]

https://doi.org/10.1190/tle42010034.1

Abstract

Seismic processing and imaging workflows have been refined over many decades to attenuate aspects of the recorded wavefield which would be improperly mapped into the image domain by legacy migration algorithms such as Kirchhoff prestack depth migration. These workflows, which include techniques such as deghosting, designature, demultiple, and regularization, have become increasingly complex and time-consuming due to the sequential fashion in which they must be tested and applied. The single-scattering (primary-only) preprocessed data are then migrated and used in extensive model building workflows, including reflection residual moveout tomography, to refine low-frequency subsurface models. Obtaining optimal results at each stage requires subjective assessment of a wide range of parameter tests. Results can be highly variable, with different decisions resulting in very different outcomes. Such workflows mean that projects may take many months or even years. Full-waveform inversion (FWI) imaging offers an alternative philosophy to this conventional approach. FWI imaging is a least-squares multiscattering algorithm that uses the raw field data (transmitted and reflected arrivals as well as their multiples and ghosts) to determine many different subsurface parameters, including reflectivity. Because this approach uses the full wavefield, the subsurface is sampled more completely during the inversion. Here, we demonstrate the application of a novel multiparameter FWI imaging technique to generate high-resolution amplitude variation with angle reflectivity simultaneously with other model parameters, such as velocity and anisotropy, directly from the raw field data. Given that these results are obtained faster than the conventional workflow with a higher resolution, improved illumination, and reduced noise, we highlight the potential of multiparameter FWI imaging to supersede the conventional workflow.

Introduction

Determining amplitude variation with angle (AVA)-compliant subsurface reflectivity and attribute models through the processing and imaging of seismic data has been commonplace for decades. Traditional workflows to obtain such products have been refined extensively over the years but still typically consist of three distinct, but fundamentally related, phases: preprocessing, model building, and imaging. While preprocessing techniques aimed at attenuating noise and correcting for acquisition inaccuracies have been a part of the workflow for a long time, historically it has been the limitations of imaging technology that have driven the extensive development of the preprocessing and model building phases.

Legacy seismic imaging methods such as Kirchhoff migration rely on the principle of stationary phase to generate the reflectivity under high-frequency asymptotic (ray-based), single-arrival, and Born approximations (Audebert et al., 1997; Bleistein et al., 2001). Historically, Kirchhoff migration has been a popular choice as it offers a relatively inexpensive way of generating depth domain reflectivity from seismic data. However, the assumptions inherent in the Kirchhoff formulation place strict requirements on the input data. The seismic data must undergo preprocessing to suppress anything other than single-scattering (primary) arrivals. Thus, arrivals such as ghosts, multiples, and the distortions of the source signature must be removed from the recorded wavefield. The imperfect subsurface sampling due to operational limitations of real acquisitions also must be resolved a priori to ensure optimum interference of the Kirchhoff migration operators.

More sophisticated seismic imaging techniques relax some of these assumptions. Beam migration also relies on the method of stationary phase as an imaging condition with ray-based and Born approximations, but it can account for multipathing through slant stack analysis on the input data (Hill, 2001; Notfors et al., 2006). However, the presence of the ray-based approximation still necessitates relatively smooth models of subsurface parameters to achieve the stable ray tracing required for generation of the migration operator Green's functions. Relaxing both the single-pathing and ray-based approximation is achievable through wavefield extrapolation techniques, where these fall into two main categories: one-way wave equation extrapolators (WEM) (Claerbout, 1971) and two-way wave equation extrapolators (reverse time migration [RTM]) (Baysal et al., 1983; Bednar et al., 2003). All of these techniques, however, have at their core the single-scattering Born approximation.

Thus, the extensive seismic preprocessing workflow phase was born (pun intended) out of the limitations of early seismic imaging methods still used today. A plethora of preprocessing techniques specializing in deghosting (e.g., Poole, 2013), internal and free surface demultiple (Verschuur et al., 1992; Weglein et al., 1997; Amundsen, 2020), designature (Lee et al., 2014), and regularization (Xu et al., 2005) were developed to ensure the input to these migration schemes satisfied their inherent approximations and improved the quality of the imaged result. Each of these stages in the preprocessing workflow must be tested, run in production, and the quality of the results checked prior to the commencement of the next stage. Consequently, this phase can be extremely time-consuming. Extensive care must also be taken to ensure each stage attenuates only the intended aspect of the wavefield, leaving the primary signal unharmed.

[1]DUG Technology, Perth, Western Australia. E-mail: jamesm@dug.com; timb@dug.com; karend@dug.com; alexp@dug.com.
[2]DUG Technology, London, UK. E-mail: tomr@dug.com; garyh@dug.com.

DOI:10.1190/tle42010034.1

Thus, subjective judgements are made to find the right balance of primary preservation and "noise" removal. This is unfortunate because, if used correctly, the discarded parts of the wavefield can provide additional illumination and, therefore, a more complete understanding of the subsurface.

Regardless of the migration algorithm chosen, an accurate understanding of subsurface model parameters, such as velocity, is required to ensure the proper focusing of seismic events during imaging. Errors in these model parameters cause suboptimal migration operator focusing and interference, resulting in the mispositioning of seismic events, noise, and a reduction in resolution. The inability of the migration algorithms to correct for (or be robust to) errors in the model parameters necessitated the model building phase, and so the conventional workflow of preprocessing, model building, and imaging became the standard approach for decades.

Obtaining accurate subsurface models for imaging during the model building phase is nontrivial. Over the past decade, full-waveform inversion (FWI) (Tarantola, 1984; Plessix, 2006; Warner et al., 2013) has become an industry-standard technique for high-resolution model building to invert for parameters such as velocity, anisotropy (Cheng et al., 2016), and Q-absorption (McLeman et al., 2018) using raw field data. Prior to its widespread adoption, techniques to refine low-frequency models such as semblance picking (Hubral and Krey, 1980), refraction tomography (White, 1989), residual moveout (RMO) reflection tomography (Stork, 1992), and well-based constraints were relied upon in complex and extensive model building workflows to obtain the optimal subsurface models for migration. FWI implementations traditionally have focused on transmitted waves, the depth of penetration of which is limited by the maximum recorded offset and the geologic setting. This has initially restricted the applicability of FWI to only the shallower parts of the model, which are typically above the target reservoir of interest. Therefore, RMO reflection tomography has still been required to update the deeper parts of the model. Such tomographic approaches have comparatively limited resolution, require the preprocessing of the seismic data to obtain high-quality RMO picks, and become unreliable in complex geology where the ray-based approximation fails.

The use of RMO reflection tomography, however, is often not just limited to updating the deeper parts of the model when FWI is part of the model building workflow. FWI implementations typically use the square of the L2-norm as the inversion objective function and apply local optimization methods (Nocedal and Wright, 2006) to minimize it. Such approaches are not well suited to capture the time shifts between the modeled and observed data due to their oscillatory nature. The highly nonlinear nature of the objective function means that for large relative time shifts, local optimization techniques will converge to a local minimum, resulting in an incorrect solution (Virieux and Operto, 2009). This has been termed the "cycle-skipping" problem and has necessitated robust, low-frequency starting models for FWI. Such starting models typically are obtained through techniques such as RMO reflection tomography and guided/surface wave inversion (Miao et al., 2017) for the near surface.

Methods to overcome cycle skipping in FWI and limit the need to perform ray-based tomography have been developed (Operto et al., 2004; Luo and Sava, 2011; Engquist and Froese, 2014; Métivier et al., 2016a, 2016b, 2016c; Warner and Guasch, 2016; Zhang et al., 2018; Messud et al., 2021). With robust, high-resolution models of the shallower section now obtainable from FWI using the raw transmitted arrivals and simpler starting models, we next must turn our attention to the deeper parts of the models.

Including reflections in FWI (Yao et al., 2020) provides us with the opportunity to not just invert for model parameters such as velocity at depth, but also to generate reflectivity as an interpretable product. Because FWI accepts the raw field data as input, including both transmission and reflection arrivals, it can make use of the ghosts and multiples to invert for a high-resolution image in an iterative least-squares sense. A common approach to obtaining such results from FWI is to include the reflections in a single-parameter inversion to high frequency (Letki et al., 2019), of which the derivative forms the pseudo-reflectivity image (Kalinicheva et al., 2020; Zhang et al., 2020). It has been shown that such an approach can deliver excellent fast-track structural images; however, a priori assumptions about density call into question their amplitude fidelity, as does the use of internal amplitude normalization schemes to overcome the unknown scaling of the source wavelet. The generation of imaged results directly from FWI using the raw field data as input is referred to as "FWI imaging."

Alternative techniques to FWI imaging that include multiple energy to determine a reflectivity image, such as via RTM, have been restricted to free-surface multiples only and have often suffered from crosstalk noise between the various orders of multiples (Yang et al., 2015). Iterative methods to suppress such crosstalk have proven successful via least-squares migration (LSM), but these methods ultimately make use of the Born approximation and require a preprocessing scheme to robustly separate the primaries and multiples without damaging either (Wong et al., 2014). An approach using WEM and a deconvolution-based imaging condition was proposed (Whitmore et al., 2010), but it is also restricted to free-surface multiples and one-way propagators, and requires robust separation of the upgoing and downgoing wavefields. In addition, the velocity model supplied to such schemes must be highly accurate or the multiple energy will not be fully removed from the final reflectivity image. Joint-migration inversion (JMI) is an LSM approach that iteratively updates the reflectivity and velocity models. Thus, it lifts the restriction of an accurate starting model and does not require the separating of primaries and multiples a priori (Berkhout, 2012). However, JMI approaches rely on one-way wave equation propagators, so some aspects of the recorded wavefield, such as transmission waves, cannot be properly utilized to improve the subsurface estimates of velocity, anisotropy, and Q that are vital to obtain high-resolution true-amplitude reflectivity models.

The FWI imaging formulation, on the other hand, offers the potential to use all orders of free-surface and internal multiples, as well as all reflected and transmitted waves, to determine subsurface model parameters, including reflectivity. Such a reflectivity could be generated acoustically (Wu and Alkhalifah, 2015; Yang et al., 2020; Wei et al., 2021). The determination of AVA properties in a cascaded workflow via FWI imaging with the elastic wave

DOI:10.1190/tle42010034.1

equation has been demonstrated successfully but comes with a comparatively higher compute cost (Wang et al., 2021).

Here, we demonstrate the potential of a novel multiparameter FWI imaging method to simultaneously obtain a variety of subsurface properties such as AVA reflectivity, velocity, and anisotropy using the raw field data as input. The AVA reflectivity is fit for both structural and amplitude analysis, with reduced noise, improved illumination, and higher resolution than is achievable with standard migration tools. Using FWI imaging, the conventional workflow phases of preprocessing, model building, and imaging are performed simultaneously with a greatly reduced turnaround time.

Method

The key to breaking the cycle of preprocessing, model building, and imaging is the ability to obtain a well-focused AVA-compliant reflectivity directly from the imaging phase using the raw field data as input while simultaneously correcting errors in the supplied model parameters as part of the estimation of the reflectivity.

The first step of the FWI imaging process is to obtain a reasonable starting model. In complex geologic settings, obtaining an initial set of models that possess the required accuracy to avoid cycle skipping in FWI is nontrivial. To reduce the reliance of the FWI imaging approach on RMO tomography and by extension the preprocessing phase, we derive a set of model parameters via FWI using the Kantorovich-Rubinstein (KR) objective function found in multidimensional optimal transport formulations (Métivier et al., 2016b; Messud et al., 2021; McLeman et al., 2022b). This objective function provides a misfit measure between two data sets that can capture not only amplitude differences but also quantifies the magnitudes of shifts between the two signals in time and space. This kind of measure performs well with the large initial kinematic errors that we are aiming to resolve.

The KR norm is given as follows:

$$KR\left(d_{mod},\, d_{obs}\right) = \max_{\varphi} \int_{X} \varphi(x)\left(d_{mod}(x) - d_{obs}(x)\right)dX, \qquad (1)$$

subject to the constraints of

$$|\varphi(x) - \varphi(x')| \le \gamma(x,x') \qquad (2)$$

and

$$|\varphi(x)| \le \lambda, \qquad (3)$$

where d_{mod} are the modeled data that have been synthesized through the two-way wave equation, d_{obs} are the recorded data, and x represents a multidimensional coordinate. Equation 2 is the 1-Lipschitz constraint which limits changes in $\varphi(x)$ spatially and temporally to vary slower than γ. Equation 3 is related to how far a signal can be shifted in time and space and represents a maximum bound on the amplitude of φ, given by λ.

The next step in the FWI imaging process is to obtain a robust true-amplitude estimation of the source wavelet. An incorrect source amplitude will result in incorrect estimation of the primary signal and the suboptimal use of multiple and ghost arrivals. Approaches for determining a source wavelet for FWI via, for example, near-field hydrophones (NFHs) are preferred but require care to guarantee an amplitude match between the modeled and observed data because there will be differences in sensitivities between the NFHs and streamer or node hydrophones. Therefore, the wavelet ambiguity must be resolved. Our approach starts with an initial full-bandwidth estimate of the source wavelet derived from gun-array modeling or NFH data. The bulk scaling and lower-frequency behavior of this wavelet is refined using a shot-by-shot least-squares direct-arrival inversion in FWI matching the modeled and observed data in order to account for variations in receiver sensitivities. Obtaining robust estimates of the source signature solely from a direct-arrival inversion at higher frequencies (above approximately 30 Hz) is nontrivial due to array effects, and so it is only used here as a means to perform calibration to overcome receiver sensitivity discrepancies rather than as a means to derive a full-bandwidth source wavelet.

With this preliminary work done, FWI imaging can proceed with a simultaneous inversion to determine a true-amplitude reflectivity and other model parameters (such as velocity) using the square of the L2-norm as the objective function. The novel FWI imaging approach presented here makes use of an augmented acoustic wave equation (McLeman et al., 2021), which in the isotropic case may be written as

$$\frac{1}{c^2}\frac{\partial^2 u}{\partial t^2} + \sum_{j=0}^{m} \nabla r_j \cdot d_j \nabla u - \nabla^2 u = \rho s \delta\left(x - x_0\right), \qquad (4)$$

where c is the P-wave velocity, u is the pressure wavefield, d is a directivity term, ρ is the density, s is the source term, x_0 is the source position, and m is an integer that controls the number of AVA-related terms to include in the wave equation. The vector ∇r_j terms strongly affect the dynamics and can add AVA-like behavior. The directivity terms are computed from the forward wavefields during propagation and the orientation of the reflectors. The ∇r_j terms are initiated with starting models r_j (if available) or are otherwise initially set to zero. It is important to note that when inverting for the vector ∇r_j components directly, one must take care to ensure that the curl operation applied to this vector should always be zero; otherwise, it will not represent a conservative field. Alternatively, one could guarantee this by inverting for r_j directly. Although for simplicity of exposition we have only presented the isotropic case, this formulation readily extends to any anisotropic symmetry.

As FWI imaging proceeds, the r_j terms and model parameters (such as velocity) are simultaneously updated to minimize the L2 misfit. The ∇r_j terms are important for forming the scattering interfaces needed to generate the reflection tomographic term in the FWI update kernel, thus allowing for velocity updates from the reflection data.

Due to the number of parameters being inverted for in the FWI imaging scheme, it is imperative that a robust optimization scheme is considered. Multiparameter inversion challenges such as parameter crosstalk and parameter scaling must be addressed.

Our approach uses L-BFGS, a quasi-Newton second-order optimizer that seeks to estimate a diagonal plus low-rank approximation to the Hessian, combined with an adaptive-gradient-like approach that helps to overcome these issues (McLeman et al., 2021).

The solutions of wave equation 4 will generate modeled data that contain all multiples and ghosts, and have an imprint of the source wavelet, including directional effects if desired. All multiples and ghosts therefore contribute to improved construction of the reflectors because they carry additional observations that the inversion demands must be consistent with the generated reflectivity and the kinematics. While all of these traditionally undesirable aspects of the wavefield are present in the input data, the act of inverting for the reflectivity terms means that they are mapped correctly into the final imaged result, rather than appearing as noise or artifacts. Thus, FWI imaging is handling the conventional workflow phases of preprocessing, model building, and imaging simultaneously and naturally in a single operation.

The application of this novel FWI imaging approach to produce velocity and intercept reflectivity simultaneously was shown by Rayment et al. (2022a), and its application at high frequency was demonstrated by Rayment et al. (2022b). It is important to note, however, that with a robust optimization scheme such as the one used here, it is possible to include additional model parameters, such as anisotropy, in the inversion. Indeed, a simultaneous three-parameter FWI imaging approach to generate velocity, epsilon anisotropy, and intercept reflectivity using the entire recorded wavefield was shown in McLeman et al. (2022a).

Results: Australian North West Shelf

Our first example is a 2006 vintage conventional towed-streamer data set from approximately 115 km northwest of Barrow Island. The survey consisted of a dual-source, eight-streamer configuration with 6 km maximum offset. There are rapid shallow velocity variations caused by localized channel features, which are difficult to resolve through tomographic methods. The initial velocity model was built from an existing regional model followed by diving-wave-only tilted transverse isotropy FWI increasing in frequency from 3 to 8 Hz with an observed maximum penetration depth of approximately 2 km.

To obtain refined models of seismic anisotropy from the existing regional models, a simultaneous triple-parameter FWI imaging approach was next performed up to a frequency of 16 Hz using a frequency-stepping approach starting from 8 Hz to generate intercept reflectivity, velocity, and epsilon. The input data at this stage were the raw field data containing both reflected and transmitted waves as well as their ghosts and multiples. Epsilon was constrained during the inversion using a structurally oriented smoothing preconditioner (Fehmers and Höcker, 2003). The refinement of the delta anisotropy was achieved through calibration to well markers in the survey area.

Figures 1a and 1b show the initial velocity and epsilon models overlain on their respective Kirchhoff prestack depth migrations (PSDMs) for quality control purposes. Figures 1d and 1e show the equivalent images but with the updated models. Both the updated velocity and epsilon models demonstrate good geologic conformance. Figure 1c shows a zoom of an inline Kirchhoff PSDM result using the initial models with the well marker (yellow) for the key horizon shown; the well-tie improvement using the updated models is evident in Figure 1f. It is important to note that although inverting simultaneously for epsilon in the FWI imaging scheme was successful on this data set, in general the level of success will vary depending on the survey design (e.g., maximum offset) and geologic setting.

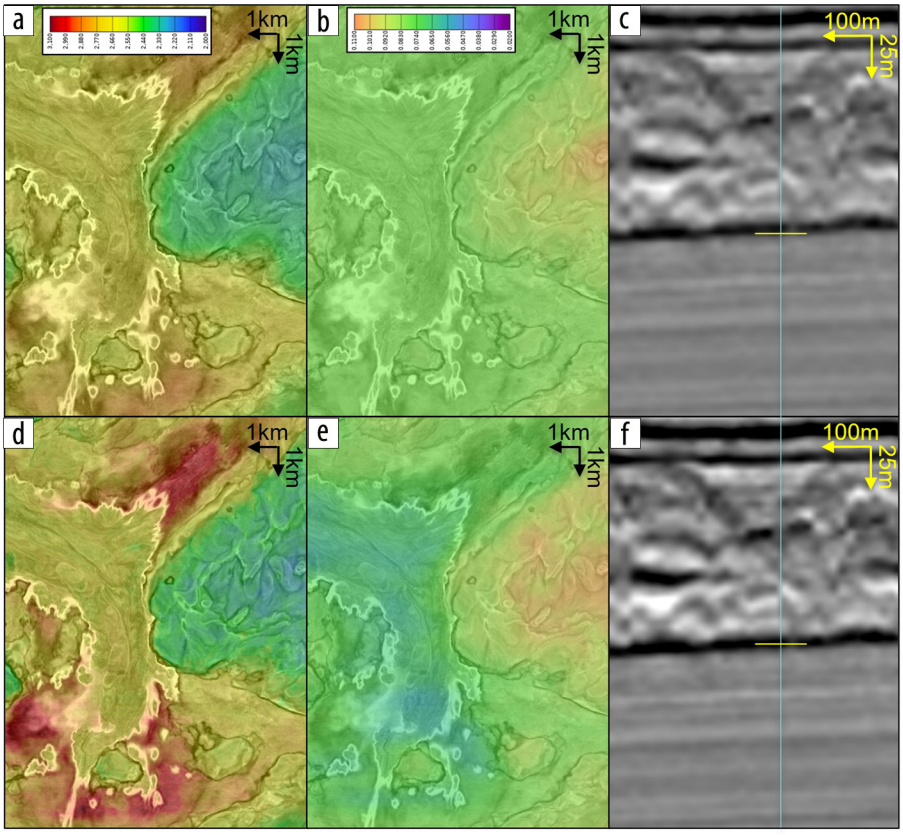

Figure 1. Kirchhoff PSDM stacks with initial (a) velocity and (b) epsilon models overlaid, and (c) their associated horizon and well marker (yellow line). Equivalents for the updated models are shown in (d), (e), and (f).

Finally, from a starting frequency of 16 Hz, a simultaneous two-parameter FWI imaging approach was applied using the frequency continuation strategy of 20, 30, 45, 65, and finally 85 Hz to determine higher-resolution velocity and intercept reflectivity models. For efficiency, the number of input shots was increased from 1/8 at the starting frequency to all the available shots at the final frequency. For this two-parameter inversion stage, a 45° outer mute was

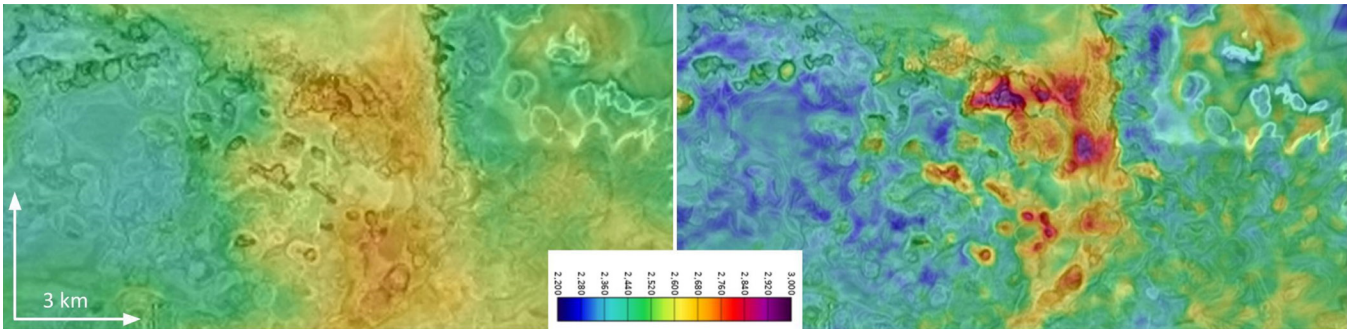

Figure 2. Depth slices at 2 km for (a) the initial velocity model overlain on a Kirchhoff PSDM stack and (b) the updated FWI model overlain on its corresponding Kirchhoff PSDM stack.

applied so only the reflection arrivals were considered.

For demonstration purposes only, a traditional Kirchhoff PSDM was run using processed input data to produce image gathers and stacks to highlight the improvement yielded by the updated models, where the stacks are overlain with their respective initial and updated velocity models. A comparison between the initial velocity model and the velocity derived from 85 Hz FWI imaging at a depth of 1.95 km can be found in Figure 2. FWI imaging has delivered a significant increase in spatial resolution, with the localized velocity anomalies well delineated by the FWI-derived model. Figures 3a and 3b also show clear geologic conformance with the updated velocity model, as well as an improvement in structural simplicity brought about by resolving the velocity anomalies in the overburden. Figures 3c and 3d show Kirchhoff image gathers before and after the model updates, respectively. Reduction in RMO is evident when using the FWI updated models for conventional imaging. Figure 3b also demonstrates a good tie between the inverted velocity and the well checkshots.

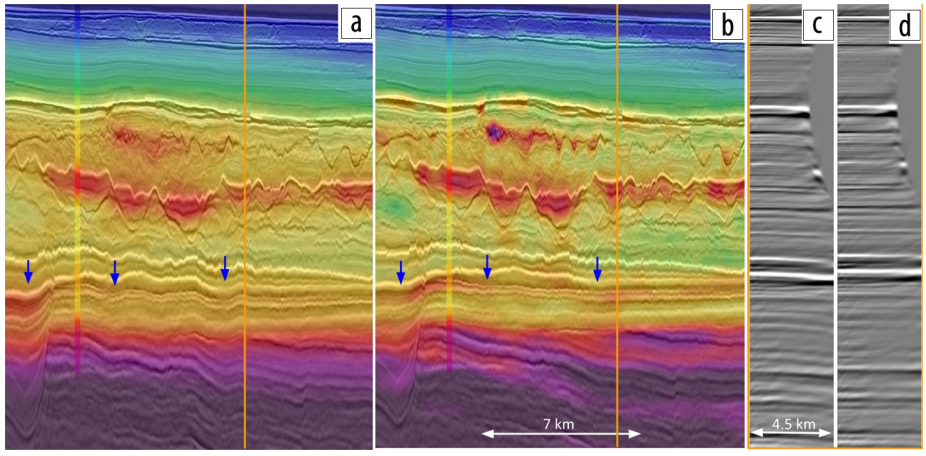

Figure 3. (a) Initial FWI velocity model overlain on its Kirchhoff PSDM stack, (b) the updated FWI model overlain on its corresponding Kirchhoff PSDM stack, (c) Kirchhoff PSDM image gathers using the initial models, and (d) with the updated models.

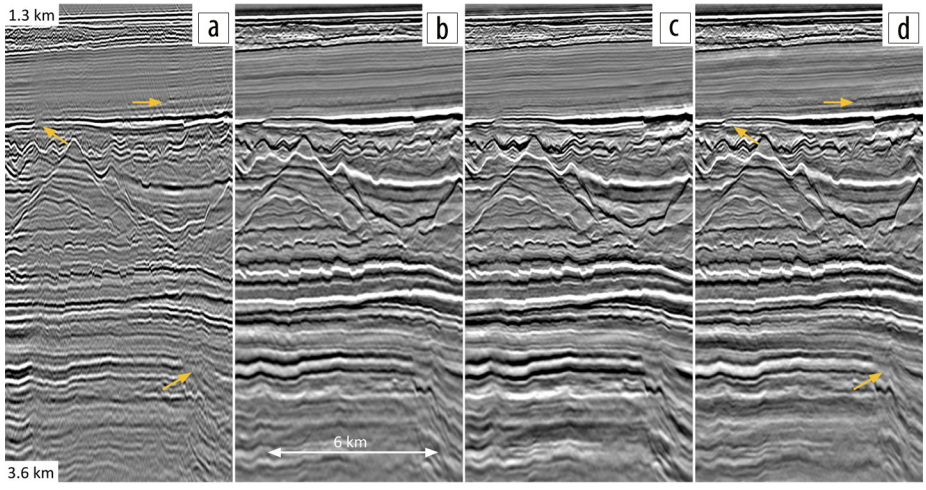

Figure 4. Crossline section through (a) Kirchhoff PSDM using raw field data, (b) Kirchhoff PSDM using preprocessed data, (c) LS-RTM using preprocessed data, and (d) FWI-derived intercept reflectivity using raw field data.

The intercept reflectivity output of the FWI imaging process is shown in Figures 4d, 5c, and 5f. For comparison, results of a Kirchhoff PSDM using raw field data, a Kirchhoff PSDM using preprocessed data, a least-squares RTM (LS-RTM) using preprocessed data, and the FWI-imaging-derived intercept reflectivity using raw field data are shown in Figures 4a, 4b, 4c, and 4d, respectively. To make the comparison fair, both the Kirchhoff and LS-RTM inputs were high-cut filtered to a frequency of 85 Hz, the same input filter used in FWI imaging, and used the FWI-imaging-derived velocity model. Figure 5 demonstrates a similar comparison but through two depth slices. As one might expect, LS-RTM has delivered an improvement in spatial resolution over the Kirchhoff approach. Remarkably, the FWI-imaging-derived reflectivity demonstrates even further improvement in spatial resolution. Complex structures are better delineated in both the inline and depth slices in the FWI imaging result. When comparing Figures 4a and 4d, both Kirchhoff and the FWI imaging approach used the raw field data as input, but the FWI imaging approach shows no evidence of multiple, ghost, or signature leakage, and it is also zero-phased. The orange arrows in Figure 4a highlight areas of poor illumination, residual multiple, and migration noise due to the irregular acquisition patterns that

DOI:10.1190/tle42010034.1

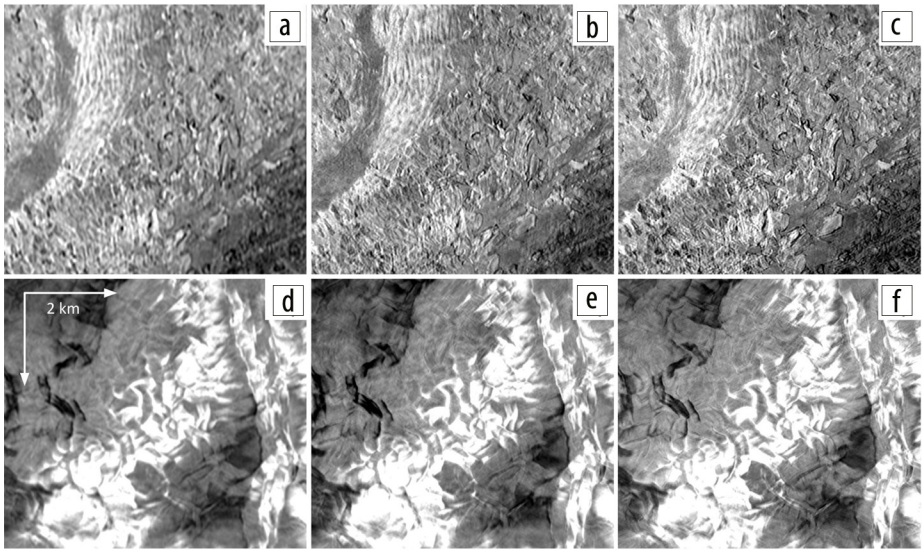

Figure 5. Depth slice at 1.5 km through (a) Kirchhoff PSDM using preprocessed data, (b) LS-RTM using preprocessed data, and (c) FWI-derived intercept reflectivity using raw field data. Panels (d), (e), and (f) are the same comparisons at 2.6 km depth.

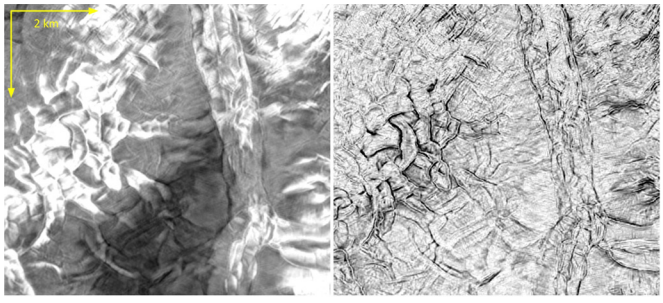

Figure 6. Depth slice at 1.8 km through (a) the intercept reflectivity and (b) the horizontal intercept reflectivity.

are resolved in Figure 4d. This highlights the success of the FWI imaging approach in simultaneously performing deghosting, designature, demultiple, model building, and least-squares imaging.

Because the derived reflectivity in the FWI imaging approach is a vector quantity, we can construct a reflectivity image from the different vector components. For example, one can consider the norm of the x and y direction reflectivity to generate a "horizontal reflectivity" image. This is shown in Figure 6. Channel boundaries and fault structures are accentuated to provide further insight into complex structures.

A shot gather modeled by FWI at the final iteration and the observed shot gather are shown in Figures 7a and 7b, respectively. An overlay of the observed data (color) and the modeled data (positive wiggle) is shown in Figure 7c, with a zoom around the multiple energy shown in Figure 7e. The modeled data given by the positive black wiggle aligns with the blue color in the observed gather overlay, meaning that the kinematics are well aligned. The amplitude spectra comparing the modeled and observed data can be found in Figure 7d and demonstrates that they match well over the inversion bandwidth. The derived model parameters and reflectivity clearly produce modeled data that matches the observed data closely when considering both primary and multiple kinematics and dynamics.

It is clear from the results presented in Figures 4–6 that FWI imaging can produce excellent structural images of reflectivity that are superior to both Kirchhoff and LS-RTM in terms of resolution. However, for it to replace the conventional workflow, one must also assess its amplitude fidelity and suitability for AVA analysis. In Figures 8d–8f, we see the result of using the FWI imaging approach to simultaneously determine near, mid, and far reflectivity angle stacks, and velocity. The comparison of the angle stacks derived from FWI imaging with those derived from a conventional Kirchhoff migration is shown in Figures 8a–8c. The velocity model used for the Kirchhoff migration was the same as that derived from the FWI imaging approach. We can observe that the amplitude trends with angle for the Kirchhoff and FWI imaging results are similar throughout the section. However, we note a reduction in noise on the near stack in the FWI-imaging-derived result. This is likely a result of residual near angle multiple, present after preprocessing the data for Kirchhoff migration, manifesting as noise in the image domain. Residual near angle multiple can be notoriously difficult to remove without damaging the primary signal. However, this is not a problem for FWI imaging; because no demultiple is required a priori, it uses the primaries, multiples, and ghosts as part of the imaging procedure to more completely sample the subsurface during the inversion.

Because the FWI imaging approach used to generate angle stacks is derived from the acoustic wave equation, the significance of elastic effects (such as converted waves) on the amplitude fidelity of derived AVA products must be considered. It has been demonstrated (e.g., Yang et al., 2017; Warner et al., 2022) that using acoustic FWI when offset or angle partitioning the input data (or even during the inversion with a modified objective function) can provide a true and direct measure of the conventional AVA properties (such as intercept and gradient), just as we would expect to derive from the traditional acoustic Kirchhoff migration workflow. Both the Kirchhoff and FWI imaging methods to derive angle stacks preserve amplitudes, but this preservation occurs in different domains and one can easily convert between them. Thus, FWI-imaging-derived angle stacks can then be used in the conventional manner to interpret lithology and pore content. The fact that we are using an acoustic formulation of FWI does not prevent us from extracting elastic properties.

To quantitatively measure the similarity between the Kirchhoff AVA trend and the FWI imaging AVA trend, AVA synthetics were computed using well data. Figure 9 shows a comparison between the well synthetic modeled responses to the Kirchhoff PSDM angle stacks and the FWI-imaging-derived angle stacks. The V_P/V_S ratio and P-impedance derived from the two approaches and the well data are also shown in Figure 9. We can see that despite the variable V_P/V_S ratio, the FWI imaging results accurately capture the expected decrease in amplitude with angle at the depth highlighted. The derived V_P/V_S ratio and P-impedance also follow the well trend

closely. This highlights the ability of FWI imaging to generate AVA-compliant reflectivity directly from the raw field data.

Results: Gulf of Mexico

The numerous, complex salt structures in the Gulf of Mexico have long proven a challenge for conventional seismic acquisition, processing, and imaging. The increased offset and azimuthal coverage of ocean-bottom node (OBN) acquisition compared to narrow-azimuth towed streamer has seen it become commonplace, with wave-equation-based techniques such as RTM being essential due to complex raypathing in this geologic setting. In the following example, we compare FWI imaging with a conventional workflow including RTM for an OBN survey in the Gulf of Mexico. The FWI imaging approach started at 15 Hz and increased to the final frequency of 20 Hz.

Imaging using the receiver ghost is routine for OBN data through mirror migration of the downgoing wavefield. This approach provides increased illumination of the near surface compared to the upgoing wavefield. Its use, however, still requires some degree of preprocessing. Figure 10 shows the results of a mirror RTM of the downgoing wavefield processed through a conventional workflow including deghosting, designature, demultiple, and model building.

Figure 11 shows the results of FWI imaging when simultaneously producing improved velocity and intercept reflectivity models from the raw pressure field data (no wavefield separation) for the same acquisition. No preprocessing was required since primaries, ghosts, and all orders of multiples are used in the imaging. There is a clear improvement in subsalt imaging and illumination using FWI imaging due to the iterative least-squares nature of the algorithm and the use of the full wavefield, including complex wavepaths such as prismatic waves. Illumination of the near surface is comparable between these results, which indicates that FWI has implicitly used the receiver ghost to derive the reflectivity output. This is further reinforced by Figure 12, which shows a conventional RTM of the same raw field data using the same FWI-imaging-derived velocity model. There are clear gaps in illumination in the shallow section, especially in the highlighted region where a receiver is missing. Source ghost

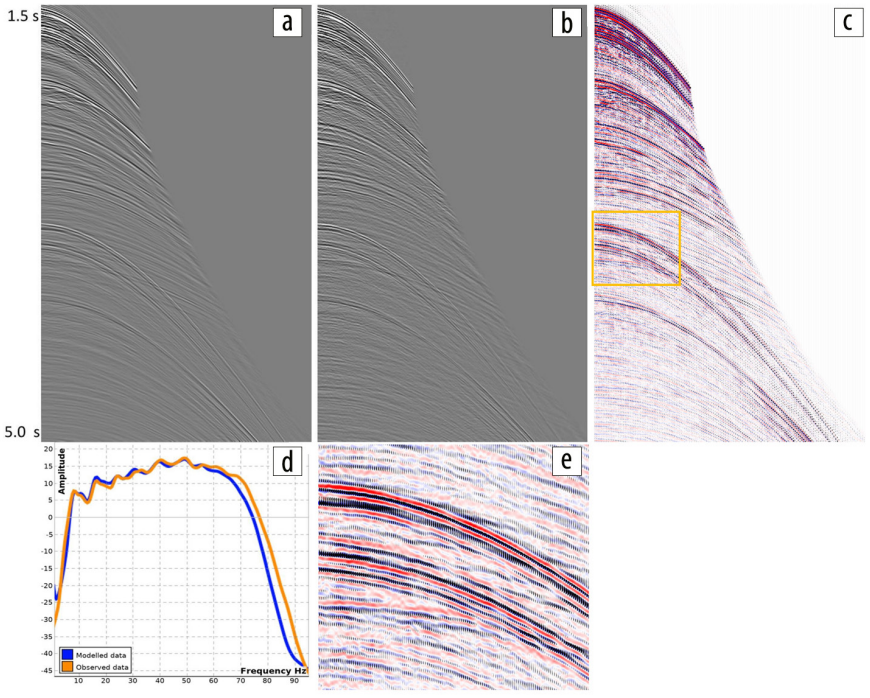

Figure 7. (a) Shot gather modeled by FWI at the final iteration, (b) the observed data shot gather, (c) the observed data (color) overlaid with the modeled data (wiggle), (d) amplitude spectra comparing the modeled and observed data, and (e) a zoom of the overlay.

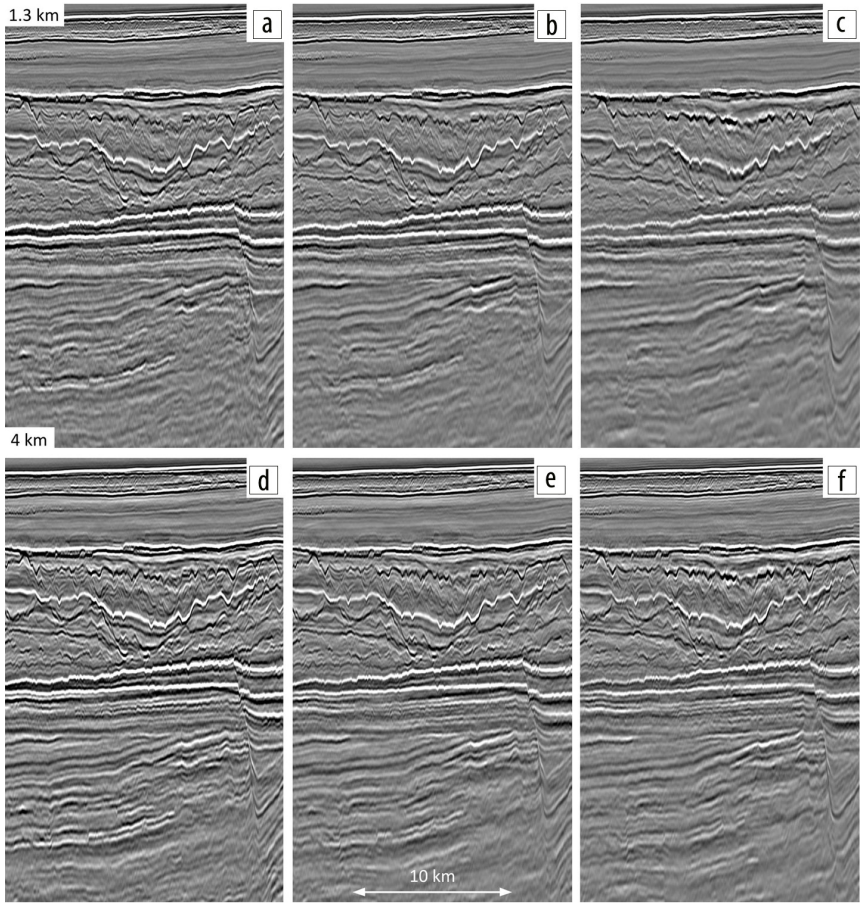

Figure 8. (a) Near, (b) mid, and (c) far angle stacks generated by Kirchhoff migration using preprocessed data. FWI imaging angle stacks derived from raw field data are shown in (d), (e), (f).

DOI:10.1190/tle42010034.1

DOI:10.1190/tle42010034.1

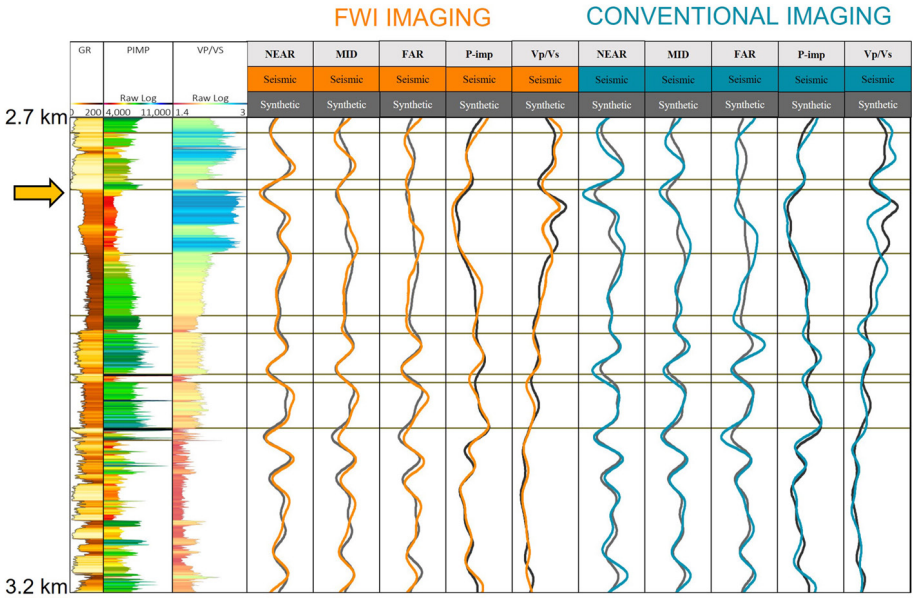

Figure 9. Well logs and AVA synthetics (gray) compared to FWI imaging (orange) and Kirchhoff PSDM (blue) responses for near, mid, and far angle ranges as well as their derived P-impedance and V_P/V_S ratio.

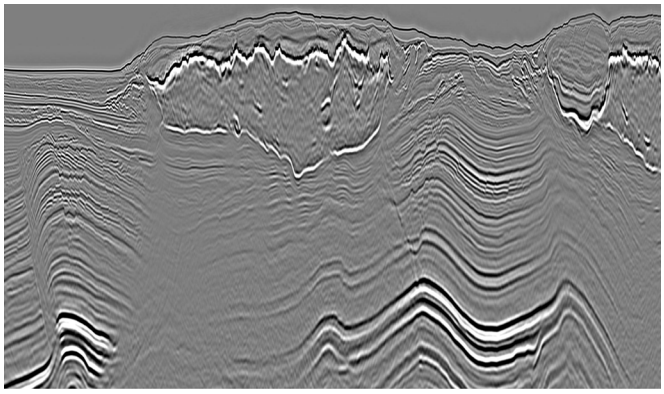

Figure 10. Legacy downgoing mirror RTM stack using preprocessed input data and velocity model derived from conventional model building.

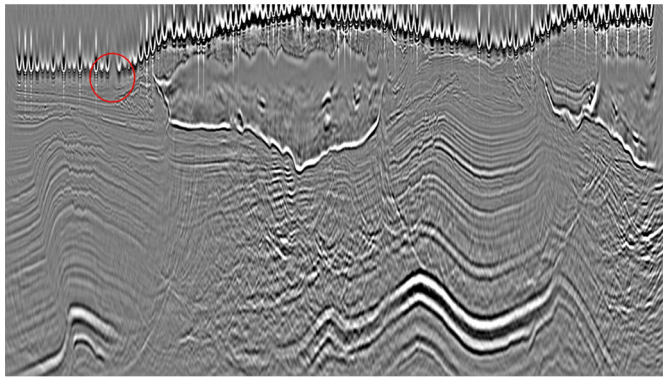

Figure 12. Conventional RTM stack using raw field data as input and the FWI-imaging-derived velocity model.

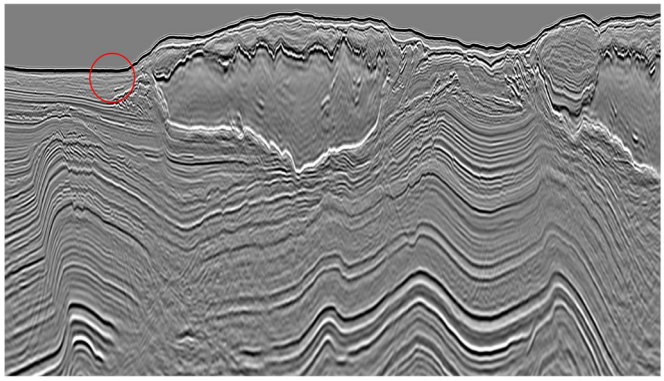

Figure 11. FWI imaging result using raw field data as input.

energy is visible, particularly at the water bottom, and multiples obscure the deeper targets. The fact that such issues are absent in the FWI imaging result demonstrates the power of this technique to utilize free-surface multiples and ghosts.

Conclusions

The multiparameter FWI imaging examples presented here demonstrate that true-amplitude reflectivity and subsurface model parameters, such as velocity and anisotropy, can be generated simultaneously. The resulting reflectivity is fit for both structural and amplitude analysis including quantitative interpretation products such as AVA stacks. The model parameters (e.g., velocity) determined simultaneously by FWI imaging were also shown to provide an improvement when used for conventional imaging techniques, such as Kirchhoff PSDM. Comparisons of the FWI imaging reflectivity with Kirchhoff and LS-RTM results highlighted an impressive uplift in resolution and illumination relative to these methods. FWI imaging has demonstrated the potential to generate AVA products directly from raw field data while simultaneously performing the model building in a less subjective way. As a result, it would be remiss of us not to ask whether it is time to set aside the old subjective workflow of preprocessing, model building, and imaging and instead embrace a new era of seismic imaging directly from raw field data? TLE

Acknowledgments

The authors would like to thank DUG Technology for permission to present these results, Multi-Client Resources (MCR) for permission to use the BEX MC3D data set, and the reviewers for their helpful comments and suggestions.

Data and materials availability

Data associated with this research are confidential and cannot be released.

Corresponding author: jamesm@dug.com

References

Amundsen, L., 2020, Review of up-down deconvolution and multidimensional deconvolution for designature/free-surface demultiple of OBN seismic data: 90th Annual International Meeting, SEG, Expanded Abstracts, 3093–3098, https://doi.org/10.1190/segam2020-3417830.1.

Audebert, F., D. Nichols, T. Rekdal, B. Biondi, D. E. Lumley, and H. Urdaneta, 1997, Imaging complex geologic structure with single-arrival Kirchhoff prestack depth migration: Geophysics, **62**, no. 5, 1533–1543, https://doi.org/10.1190/1.1444256.

Baysal, E., D. D. Kosloff, and J. W. C. Sherwood, 1983, Reverse time migration: Geophysics, **48**, no. 11, 1514–1524, https://doi.org/10.1190/1.1441434.

Bednar, J. B., K. Yoon, C. Shin, and L. Lines, 2003, One way vs two way wave equation imaging — Is two-way worth it?: 65th Conference and Exhibition, EAGE, Extended Abstracts, https://doi.org/10.3997/2214-4609-pdb.6.B11.

Berkhout, A. J., 2012, Combining full wavefield migration and full waveform inversion, a glance into the future of seismic imaging: Geophysics, **77**, no. 2, S43–S50, https://doi.org/10.1190/geo2011-0148.1.

Bleistein, N., J. W. Stockwell, and J. K. Cohen, 2001, Mathematics of multidimensional seismic imaging, migration, and inversion: Springer, https://doi.org/10.1007/978-1-4613-0001-4.

Cheng, X., K. Jiao, D. Sun, and D. Vigh, 2016, Multiparameter estimation with acoustic vertical transverse isotropic full-waveform inversion of surface seismic data: Interpretation, **4**, no. 4, SU1–SU16, https://doi.org/10.1190/INT-2016-0029.1.

Claerbout, J. F., 1971, Toward a unified theory of reflector mapping: Geophysics, **36**, no. 3, 467–481, https://doi.org/10.1190/1.1440185.

Engquist, B., and B. D. Froese, 2014, Application of the Wasserstein metric to seismic signals: Communications in Mathematical Sciences, **12**, no. 5, 979–988, https://doi.org/10.4310/CMS.2014.v12.n5.a7.

Fehmers, G. C., and C. F. W. Höcker, 2003, Fast structural interpretation with structure-oriented filtering: Geophysics, **68**, no. 4, 1286–1293, https://doi.org/10.1190/1.1598121.

Hill, N. R., 2001, Prestack Gaussian-beam depth migration: Geophysics, **66**, no. 4, 1240–1250, https://doi.org/10.1190/1.1487071.

Hubral, P., and T. Krey, 1980, Interval velocities from seismic reflection time measurements: SEG, https://doi.org/10.1190/1.9781560802501.

Kalinicheva, T., M. Warner, and F. Mancini, 2020, Full-bandwidth FWI: 90th Annual International Meeting, SEG, Expanded Abstracts, 651–655, https://doi.org/10.1190/segam2020-3425522.1.

Lee, C.-C., Y. Li, S. Ray, and G. Poole, 2014, Directional designature using a bootstrap approach: 84th Annual International Meeting, SEG, Expanded Abstracts, 4253–4257, https://doi.org/10.1190/segam2014-1287.1.

Letki, L., M. Lamont, and T. Thompson, 2019, High frequency full waveform inversion as an interpretation solution: The APPEA Journal, **59**, no. 2, 904–908, https://doi.org/10.1071/AJ18123.

Luo, S., and P. Sava, 2011, A deconvolution-based objective function for wave-equation inversion: 81st Annual International Meeting, SEG, Expanded Abstracts, 2788–2792, https://doi.org/10.1190/1.3627773.

McLeman, J., T. Burgess, and T. Rayment, 2022a, FWI imaging with simultaneous anisotropy estimation: 83rd Conference and Exhibition, EAGE, Extended Abstracts, https://doi.org/10.3997/2214-4609.202210075.

McLeman, J., T. Burgess, T. Rayment, and V. Chua, 2022b, Mitigating cycle skipping in FWI through preconditioned multidimensional optimal transport: Second International Meeting for Applied Geoscience & Energy, SEG/AAPG, Expanded Abstracts, 742–746, https://doi.org/10.1190/image2022-3744903.1.

McLeman, J., T. Burgess, M. Sinha, G. Hampson, and T. Thompson, 2021, Reflection FWI with an augmented wave equation and quasi-Newton adaptive gradient scheme: First International Meeting for Applied Geoscience & Energy, SEG/AAPG, Expanded Abstracts, 667–671, https://doi.org/10.1190/segam2021-3582659.1.

McLeman, J., B. Xiao, C. Page, F. Jouno, N. Salaun, A. Roubaud, F. Perrone, 2018, Next generation shallow water resolution: Primary wave imaging and high frequency visco-acoustic full-waveform Inversion: 80th Conference and Exhibition, EAGE, Extended Abstracts, https://doi.org/10.3997/2214-4609.201801163.

Messud, J., R. Poncet, and G. Lambaré, 2021, Optimal transport in full-waveform inversion: analysis and practice of multidimensional Kantorovich-Rubinstein norm: Inverse Problems, **37**, no. 6, 065012, https://doi.org/10.1088/1361-6420/abfb4c.

Métivier, L., R. Brossier, Q. Mérigot, E. Oudet, and J. Virieux, 2016a, Increasing the robustness and applicability of full-waveform inversion: An optimal transport distance strategy: The Leading Edge, **35**, no. 12, 1060–1067, https://doi.org/10.1190/tle35121060.1.

Métivier, L., R. Brossier, Q. Mérigot, E. Oudet, and J. Virieux, 2016b, Measuring the misfit between seismograms using an optimal transport distance: Application to full waveform inversion: Geophysical Journal International, **205**, no. 1, 345–377, https://doi.org/10.1093/gji/ggw014.

Métivier, L., R. Brossier, Q. Mérigot, E. Oudet, and J. Virieux, 2016c, An optimal transport approach for seismic tomography: Application to 3D full waveform inversion: Inverse Problems, **32**, no. 11, 115008, https://doi.org/10.1088/0266-5611/32/11/115008.

Miao, X., Z. Zhou, and S. Hou, 2017, Shallow velocity and shear statics by multi-modal surface wave inversion: OBN/OBC Technologies and Applications, SEG, Global Meeting Abstracts, 5–8, https://doi.org/10.1190/obnobc2017-02.

Nocedal, J., and S. J. Wright, 2006, Numerical optimization: Springer, https://doi.org/10.1007/978-0-387-40065-5.

Notfors, C., Y. Xie, and S. Gray, 2006, Gaussian Beam migration: A viable alternative to Kirchhoff: ASEG Extended Abstracts, no. 1, 1–4, https://doi.org/10.1071/ASEG2006ab201.

Operto, S., C. Ravaut, L. Improta, J. Virieux, A. Herrero, and P. Dell'Aversana, 2004, Quantitative imaging of complex structures from dense wide-aperture seismic data by multiscale traveltime and waveform inversions: A case study: Geophysical Prospecting, **52**, no. 6, 625–651, https://doi.org/10.1111/j.1365-2478.2004.00452.x.

Plessix, R.-E., 2006, A review of the adjoint-statement for computing the gradient of a functional with geophysical applications: Geophysical Journal International, **167**, no. 2, 495–503, https://doi.org/10.1111/j.1365-246X.2006.02978.x.

Poole, G., 2013, Pre-migration receiver de-ghosting and re-datuming for variable depth streamer data: 83rd Annual International Meeting, SEG, Expanded Abstracts, 4216–4220, https://doi.org/10.1190/segam2013-0541.1.

Rayment, T., K. Dancer, J. McLeman, T. Burgess, 2022b, High-resolution FWI imaging — An alternative to conventional processing: 83rd

Conference and Exhibition, EAGE, Extended Abstracts, https://doi.org/10.3997/2214-4609.202210233.
Rayment, T., J. McLeman, K. Dancer, and T. Burgess, 2022a, Next-generation resolution through multiparameter FWI imaging: Second International Meeting for Applied Geoscience & Energy, SEG/AAPG, Expanded Abstracts, 922–926, https://doi.org/10.1190/image2022-3745707.1.
Stork, C., 1992, Reflection tomography in the postmigrated domain: Geophysics, **57**, no. 5, 680–692, https://doi.org/10.1190/1.1443282.
Tarantola, A., 1984, Inversion of seismic reflection data in the acoustic approximation: Geophysics, **49**, no. 8, 1259–1266, https://doi.org/10.1190/1.1441754.
Verschuur, D. J., A. J. Berkhout, and C. P. A Wapenaar, 1992, Adaptive surface-related multiple elimination: Geophysics, **57**, no. 9, 1166–1177, https://doi.org/10.1190/1.1443330.
Virieux, J., and S. Operto, 2009, An overview of full-waveform inversion in exploration geophysics: Geophysics, **74**, no. 6, WCC1–WCC26, https://doi.org/10.1190/1.3238367.
Wang, H., O. Burtz, P. Routh, D. Wang, J. Violet, R. Lu, and S. Lazaratos, 2021, Anisotropic 3D elastic full-wavefield inversion to directly estimate elastic properties and its role in interpretation: The Leading Edge, **40**, no. 4, 277–286, https://doi.org/10.1190/tle40040277.1.
Warner, M., J. Armitage, A. Umpleby, N. Shah, H. Debens, and F. Macini, 2022, Full-elastic AVA extraction using acoustic FWI: Second International Meeting for Applied Geoscience & Energy, SEG/AAPG, Expanded Abstracts, 907–911, https://doi.org/10.1190/image2022-3750777.1.
Warner, M., and L. Guasch, 2016, Adaptive waveform inversion: Theory: Geophysics, **81**, no. 6, R429–R445, https://doi.org/10.1190/geo2015-0387.1.
Warner, M., A. Ratcliffe, T. Nangoo, J. Morgan, A. Umpleby, N. Shah, V. Vinje, et al., 2013, Anisotropic 3D full-waveform inversion: Geophysics, **78**, no. 2, R59–R80, https://doi.org/10.1190/geo2012-0338.1.
Weglein, A. B., F. A. Gasparotto, P. M. Carvalho, and R. H. Stolt, 1997, An inverse-scattering series method for attenuating multiples in seismic reflection data: Geophysics, **62**, no. 6, 1975–1989, https://doi.org/10.1190/1.1444298.
Wei, Z., J. Mei, Z. Wu, Z. Zhang, R. Huang, and P. Wang, 2021, FWI Imaging: Revealing the unprecedented resolution of seismic data: First International Meeting for Applied Geoscience & Energy, SEG/AAPG, Expanded Abstracts, 682–686, https://doi.org/10.1190/segam2021-3583772.1.
White, D. J., 1989, Two-dimensional seismic refraction tomography: Geophysical Journal International, **97**, no. 2, 223–245, https://doi.org/10.1111/j.1365-246X.1989.tb00498.x.
Whitmore, N. D., A. A. Valenciano, W. Sollner, and S. Lu, 2010, Imaging of primaries and multiples using a dual-sensor towed streamer: 80th Annual International Meeting, SEG, Expanded Abstracts, 3187–3192, https://doi.org/10.1190/1.3513508.
Wong, M., B. Biondi, and S. Ronen, 2014, Imaging with multiples using least-squares reverse time migration: The Leading Edge, **33**, no. 9, 970–976, https://doi.org/10.1190/tle33090970.1.
Wu, Z., and T. Alkhalifah, 2015, Simultaneous inversion of the background velocity and the perturbation in full-waveform inversion: Geophysics, **80**, no. 6, R317–R329, https://doi.org/10.1190/geo2014-0365.1.
Xu, S., Y. Zhang, D. Pham, and G. Lambaré, 2005, Antileakage Fourier transform for seismic data regularization: Geophysics, **70**, no. 4, V87–V95, https://doi.org/10.1190/1.1993713.
Yang, D., R. Bansal, S. Lazaratos, J. Yan, and A. Baumstein, 2017, FWI model domain angle stacks with amplitude preservation: U.S. Patent No. US20170108602A1.
Yang, Y., J. Ramos-Martinez, D. Whitmore, A. Valenciano, and N. Chemingui, 2020, Full waveform inversion using wave equation reflectivity modelling: 81st Conference and Exhibition, EAGE, Extended Abstracts, https://doi.org/10.3997/2214-4609.202011146.
Yang, Z., J. Hembd, H. Chen, and J. Yang, 2015, Reverse time migration of multiples: Applications and challenges: The Leading Edge, **34**, no. 7, 780–786, https://doi.org/10.1190/tle34070780.1.
Yao, G., D. Wu, and S.-X. Wang, 2020, A review on reflection-waveform inversion: Petroleum Science, **17**, 334–351, https://doi.org/10.1007/s12182-020-00431-3.
Zhang, Z., J. Mei, F. Lin, R. Huang, and P. Wang, 2018, Correcting for salt misinterpretation with full-waveform inversion: 88th Annual International Meeting, SEG, Expanded Abstracts, 1143–1147, https://doi.org/10.1190/segam2018-2997711.1.
Zhang, Z., Z. Wu, Z. Wei, J. Mei, R. Huang, and P. Wang, 2020, FWI imaging: Full-wavefield imaging through full-waveform inversion: 90th Annual International Meeting, SEG, Expanded Abstracts, 656–660, https://doi.org/10.1190/segam2020-3427858.1.